Dual-Frequency High-Electric-Field Generator for MRI Safety Testing of Passive Implantable Medical Devices

Shuo Song[®], *Graduate Student Member, IEEE*, Jianfeng Zheng[®], *Member, IEEE*, Yu Wang[®], Qingyan Wang[®], Wolfgang Kainz[®], *Member, IEEE*, Stuart A. Long[®], *Life Fellow, IEEE*, and Ji Chen[®], *Senior Member, IEEE*

Abstract—In this article, an electric (E) field generator is developed to generate uniform and high-strength E-fields at multiple frequencies. The system can be used to assess the radio frequency (RF) hazards of implantable medical devices (IMDs) in magnetic resonance imaging (MRI) environments. The novel system consists of three parts: 1) a signal generating and amplifying block; 2) a four-channel feeding network; and 3) a rectangular resonator box. Mixed modes are utilized to generate locally uniform E-fields inside the rectangular resonator at both 64 and 128 MHz. RF-induced heating for two passive IMD families are evaluated using both numerical and experimental methods inside the E-field generator. These results are compared with those obtained from standard American Society of Testing and Materials (ASTM) phantom testing. The results show that the novel E-field generator is capable of evaluating RF-induced heating for passive IMDs similar to that of the ASTM phantom. Furthermore, it integrates both 1.5- and 3-T RF-induced heating tests in a single system. It is much simpler compared to the ASTM test method which needs the RF coil as a source. Consequently, this small and efficient E-field generator can be used as an alternative system for RF-induced heating tests of passive IMDs in the MRI environment.

Index Terms—Cavity model, field generator design, implantable medical device (IMD), magnetic resonance imaging (MRI).

I. Introduction

AGNETIC resonance imaging (MRI) is a widely used imaging method due to its noninvasive nature and high image quality. During the MRI procedure, radio frequency (RF) signals penetrate the human body and interact with the tissues [1], [2]. For patients with electrically conductive implantable medical devices (IMDs), the conductive parts will strongly interact with the electromagnetic (EM) fields and lead to localized RF energy deposition in tissues near the IMDs. There are numerous reports about patient burn

Manuscript received August 16, 2020; accepted September 20, 2020. Date of publication October 27, 2020; date of current version December 3, 2020. (Corresponding author: Ji Chen.)

Shuo Song, Jianfeng Zheng, Yu Wang, Qingyan Wang, Stuart A. Long, and Ji Chen are with the Department of Electrical and Computer Engineering, University of Houston, Houston, TX 77204-4005 USA (e-mail: ssong11@uh.edu; jzheng4@central.uh.edu; ywang129@uh.edu; qwang25@uh.edu; long@central.uh.edu; jchen23@central.uh.edu).

Wolfgang Kainz is with the Center for Devices and Radiological Health, Food and Drug Administration, Silver Spring, MD 20852 USA (e-mail: wolfgang.kainz@fda.hhs.gov).

Color versions of one or more of the figures in this article are available online at https://ieeexplore.ieee.org.

Digital Object Identifier 10.1109/TMTT.2020.3030789

incidents and influences on IMDs' function caused by such highly concentrated power deposition [3]–[7]. Although direct *in vivo* MRI RF-induced heating measurement methods can potentially be used for safety assessment [8], [9], *in vitro* investigation of RF-induced heating and design optimization are still needed before the IMDs can be implanted as an MR conditional device. Such MR conditional devices allow the patient to safely undergo an MRI scan under very specific conditions. In many cases, the *in vitro* measured heating data are directly used to label an IMD MR conditional [10], [11].

Currently, performing RF-induced heating tests based on the American Society of Testing and Materials (ASTM) standard requires a large-sized RF coil for each frequency to be studied and a high-power supply system together with a large shielded room. Such RF coils are available as part of MRI systems or equivalent test systems based on birdcage coils or transverse electromagnetic (TEM) coils [12], [13]. Due to potential differences in coil types and coil sizes, local incident field calibration is required [14]. Additionally, the linear variation of the E-field along the radial direction inside the ASTM phantom in a typical RF birdcage coil will limit the test region to achieve a high signal to noise ratio. The limited test region also requires accurate IMDs' positioning systems to reduce the experimental uncertainty [15].

Due to these limitations and with "new knowledge about RF-induced heating related to the presence of an implant in a patient undergoing an MRI examination," the new ASTM F2182-19e² focusing on local exposure was developed [14]. The new 19e² standard is "focusing the analysis on local exposure, rather than whole-phantom calorimetry" [16]–[19]. The in vitro test is aimed to characterize the heating behavior of the IMD family "under the well-characterized incident field," find the possible worst case conditions, and then reasonably infer, or numerically predict, the RF-induced heating in actual in vivo scenarios when an IMD is implanted inside a human body [14]. Furthermore, "the phantom geometry has been further simplified and provided only as a possible example, allowing other geometries as well" [14]. All these indicate that if one can develop a test system with well-characterized local exposure, it can also be used to assess the RF-induced heating for IMDs.

Since the test locations recommended in the ASTM standard suggest that the E-fields generated by the RF coil are mainly aligned with the bore direction, typically indicated as the

0018-9480 © 2020 IEEE. Personal use is permitted, but republication/redistribution requires IEEE permission. See https://www.ieee.org/publications/rights/index.html for more information.

z-direction, the quantitative heating measurements essentially capture the interaction of the IMD with E-fields in this direction [20]–[23]. Therefore, efficient *in vitro* assessment of RF-induced heating requires a strong local E-field and a well-characterized background heating.

Various types of field-generating equipment have been developed, for example: 1) electromagnetic compatibility (EMC) tests for active IMDs; 2) open area test of electrically powered medical devices; and 3) immunity testing of medical devices using wireless communications. A transmission line system (TLS) is recommended in the ISO 11451-2 standard [24]. This TLS uses terminated transmission line elements to generate EM fields between the conductors and the shielded structures. However, the system requires a large chamber; additionally, the radiated fields have the risk of coupling with the chamber enclosure [25]. Another TLS-based design has been proposed by McLean [26] to generate high-intensity EM fields over a wide frequency range, but the strength of the generated field dramatically changes in the test region. Groh et al. [27] reviewed other transmission line-based designs and suggested that open TEM lines, like parallel plate guides, are faced with problems of radiation and coupling with the shielded room, while enclosed TEM lines, which have a closed structure and inside radiating elements, will make the experiments complex. The gigahertz TEM cell is also widely used in EMC tests; however, the variation of the field strength will be too large to perform stable heating measurements for IMDs [28]. For medical devices, the ISO-10974 standard proposes a trough line resonator design. This device is designed to generate ultrahigh fields for testing electrically short IMDs. However, the enclosed resonator structure requires a fixed length at the desired frequency, making it not suitable for a multifrequency capable system. Other antenna-based designs, including Bilog antennas, are able to generate strong uniform fields but have the disadvantage of low power efficiency and require large chambers for operation [29].

In this article, we design, built, calibrate, test, and compare to the ASTM F2182 test method, a novel dual-frequency uniform E-field generator for 64 and 128 MHz. For practical considerations, a high-strength uniform E-field constrained to the inside of a rectangular box is desirable. The EM field in such a resonance structure can be characterized by transverse electric (TE) modes based on the cavity model [30].

In the proposed design, mixed TE modes of the rectangular resonator are used to generate uniform E-field at 64 and 128 MHz. The dimensions of the E-field generator are chosen as a tradeoff between: 1) field homogeneity for dual-frequency capability; 2) power efficiency; and 3) sufficient space to test typical IMDs. The dual-frequency-in-one design requires lumped elements' circuits to match the resonator at varying frequencies. Compared to the ASTM standard test system, using the ASTM phantom driven by an RF coil, the new design has the advantage of low cost, less sensitivity to IMD positioning error, ease of fabrication and operation, and most importantly, integration of both 1.5- and 3-T RF-induced heating tests into one single system.

The remainder of this article is organized as follows. Section II presents the design and development of the novel E-field generator, including: 1) numerical simulations; 2) experimental validation; and 3) system calibration at 64 and 128 MHz. Section III provides the numerical simulation results of the RF-induced heating for two IMD families and positioning error analysis on a selection of IMDs. RF-induced heating measurements on a selection of IMDs were performed in the E-field generator and the ASTM phantom and compared to each other in Section IV. Section V provides the discussion and Section VI presents the conclusions.

II. MULTIFREQUENCY E-FIELD GENERATOR

In this section, we describe the development of the multifrequency E-field generator system. It is followed by the calibration procedures which include both total input power calibration and local 10-cm titanium calibration procedure. The validation of the incident field generated by the system is then presented.

A. Design of the Multifrequency E-Field Generator

There are several key requirements that need to be met to accomplish reliable and efficient measurements. To meet the ASTM RF-induced heating test requirements, the E-field generator needs to 1) generate a sufficiently high E-field along the longitudinal direction of the transverse plane (*z*-direction) similar to that at the test location inside the ASTM phantom; 2) generate a uniform E-field to minimize the positioning error; 3) be accessible from the top so that the test devices can be accurately positioned and inspected; and 4) be large enough to accommodate IMDs of typical sizes used in clinical settings.

A rectangular-shaped box, shown in Fig. 1, was developed for this study. The central region of this box is then filled with gelled saline. As prescribed in the ASTM standard, the gelled saline should have a relative permittivity of 78 and an electrical conductivity of 0.47 S/m. The corresponding wavelengths for 1.5- and 3-T systems are around 45 and 22 cm, respectively. By attaching copper-clad, flexible circuit boards with excitations to the sidewalls of the box, a cavity can be formed if appropriate cavity modes treat the top/bottom surfaces as perfect magnetic conductors. The top side of the gel box is open. To generate a uniform E-field along one direction of the transverse plane (xz plane), the TE_{10} mode is utilized for 64 MHz. The dimension of 300 mm \times 300 mm is chosen along the x- and z-directions so that the resonance frequency of the TE₁₀ mode is around 64 MHz and there will be enough space to place typical IMDs. As the frequency of the 3-T MRI increases to 128 MHz, high-order modes, such as the TE₂₀ and TE₁₂ modes, will have noticeable strength.

To minimize the influence of these high-order modes, several methods are used. First, the dimensions of 300 mm \times 300 mm are chosen to suppress the higher modes, and second, a special four-way feeding network is developed. Four gaps are cut on the left and right walls near the four corners of the box. SubMiniature version A (SMA) connectors are connected to the gaps to form even and differential excitations between the front (+z) and back (-z) box walls, as shown in Fig. 1. Two gaps on the cavity's front and back walls are cut for decoupling the left (-x) and right (+x) channels. Such a feeding network ensures that only modes with major E-field components along

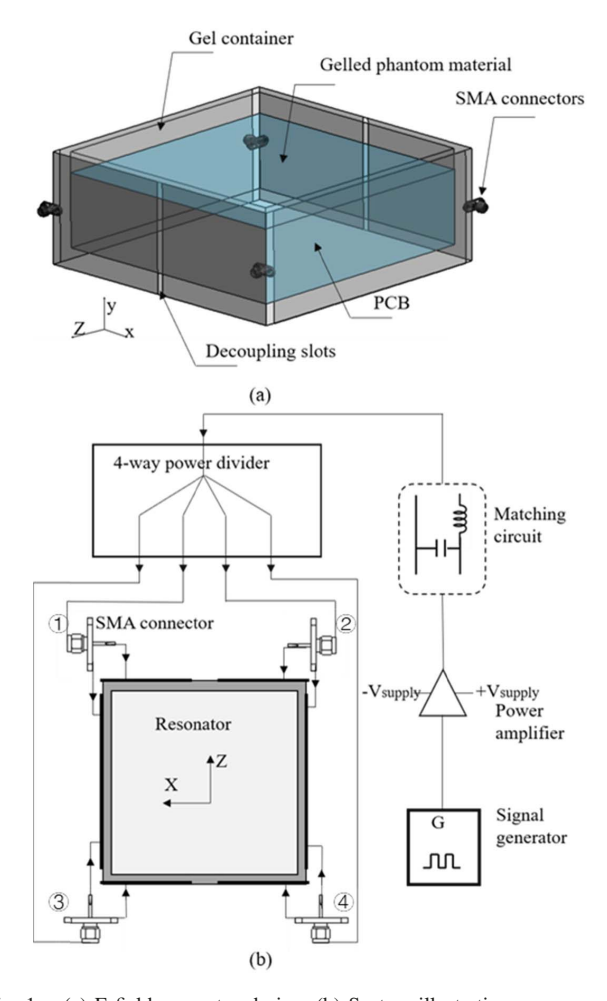


Fig. 1. (a) E-field generator design. (b) System illustration.

the z-direction can be excited and the E-field of those modes will be symmetric with respect to both the x-axis and z-axis.

Fig. 1(b) illustrates the schematic of the system. The signal from a signal generator is amplified using a power amplifier (ZHL-100W-52-S+ from Mini-Circuits, Brooklyn, NY, USA) supplied with a direct current (dc) power source. The RF signal travels through the power divider into a lumped-element matching circuit ("L" type). The output signals of a four-way power divider (H4S-0.252WWP from Meca Electronics, Denville, NJ, USA) with the same magnitude and phase are connected to SMA connectors attached on the wall using coaxial cables. A special four-way feeding network is acquired by exciting the front (+z) and back (-z) walls differentially as shown in Fig. 1(b). The front (+z) copper plates are connected to the outer conductor of the SMA connector, while the copper plates on the back (-z) wall are connected to the inner conductor of the SMA connector.

The full-wave numerical simulations are performed to assist the design. Such EM simulations were performed using the commercial FDTD software SEMCAD X (ZMT, Zurich, Switzerland). Copper plates on the acrylic box are modeled as perfect electric conductor (PEC) on a dielectric box with a relative permittivity of 2.25 and an electrical conductivity of 0 S/m. The copper plates are modeled as ideal PEC with no thickness, the wall of the acrylic box is 12.5 mm in thickness, and the box outer dimensions are 300 mm × 300 mm × 120 mm. The SMA excitations are modeled as lumped

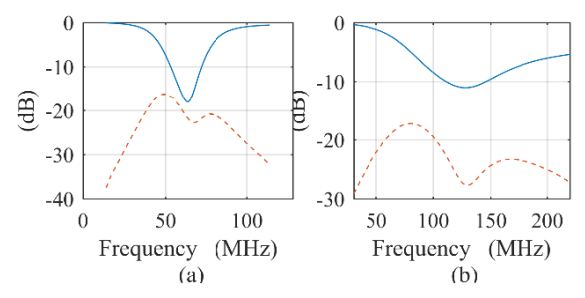


Fig. 2. S-parameters of the E-field generator for (a) 1.5 T (64 MHz) and (b) 3 T (128 MHz). Blue solid line for S_{11} and red dotted line for S_{21} .

sources, the gelled saline is modeled as a lossy dielectric material (relative permittivity = 78, electrical conductivity = 0.47 S/m), the height of the gel is 90 mm, and the grid resolution of the simulation is 2.0 mm.

The matching circuit is modeled as lumped elements in series with the sources. The broadband simulations were performed to match the resonator at 64 and 128 MHz for the 1.5- and 3-T MRI systems. As shown in Fig. 2, we observed that the S_{11} values were below -10 dB, and the S_{21} values were below -15 dB. The numbering of the ports is shown in Fig. 1. The reflection and coupling of other ports are not shown since the structure is symmetric.

Based on the designed structure, the EM simulations were performed for the two frequencies and the E-field distributions are shown in Fig. 3. The input power in the simulations is normalized to 32.52 W at 64 MHz and 13.77 W at 128 MHz, so that the induced E-field in the generator will be equivalent to the E-field at the test in a standard ASTM phantom location (around111 (64 MHz) and 91 V/m (128 MHz)) when the whole-body averaged phantom specific absorption rate (SAR) is normalized to 2 W/kg.

As shown in Fig. 3, for 1.5 T (64 MHz), the E-field distribution is similar to that of a TE₁₀ mode, whereas for 3 T (128 MHz), the E-field distribution is similar to a combination of a TE₁₀ mode and a TE₂₁mode. However, in both cases, relatively uniform E-field distribution can be achieved in the center on the E-field generator.

The Q-factor is assessed based on the stored energy and the consumed energy per period, and the comparisons of the results and those from the analytical calculation are shown in Table I.

The main loss of the system is due to the power dissipation in the gel, and the major contribution of the Q-factor is from conductivity loss as follows:

$$Q_{\rm d} = \frac{1}{\tan \delta} \tag{1}$$

$$Q_{\rm d} = \frac{1}{\tan \delta}$$

$$\tan \delta \approx \frac{\sigma}{\omega * \varepsilon_0 \varepsilon_{\rm r}}$$
(1)

where σ is the electrical conductivity of phantom material $(\sigma = 0.47 \text{S/m}), \omega$ is the angular frequency $(\omega = 2*\pi*64 \text{MHz})$ for 1.5 T; $\omega = 2 * \pi * 128 \text{MHz}$ for 3 T), ε_0 is the vacuum permittivity, and ε_r is the permittivity of the gel ($\varepsilon_r = 78$).

The Q-factor (Q_s) can be obtained using

$$Q_{\rm s} = \frac{\omega_0' U}{P_{\rm d}^{\rm ave}} \tag{3}$$

where U is the stored energy, $P_{\rm d}^{\rm ave}$ is the averaged power dissipated, and ω'_0 is the real angular frequency.

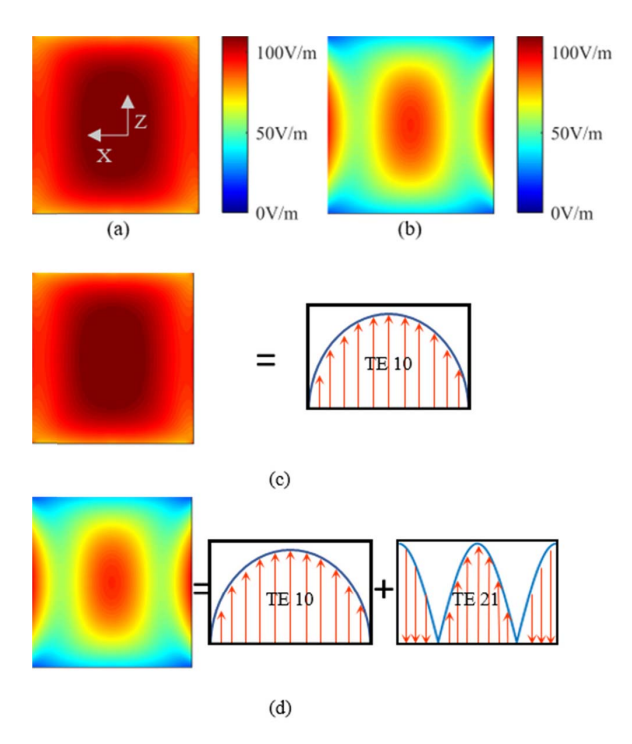


Fig. 3. Electric field distribution at the center slice of gel based on the numerical simulation. (a) Electric field along the z-direction solved using the numerical method for 64 MHz. (b) Electric field along the z-direction solved using the numerical method at 128 MHz. (c) Single mode at 64 MHz. (d) Hybrid modes of 3 T.

TABLE I
Q-FACTOR COMPARISON

	Dielectric loss/W	Frequency /MHz	Stored energy/J	$Q_{\substack{simu\label{simu}\label{lation}}}$	$Q_{theor} \ _{etical}$
64MHz	32.34	64	5.41e-8	0.67	0.61
128MHz	13.64	128	2.24e-8	1.32	1.17

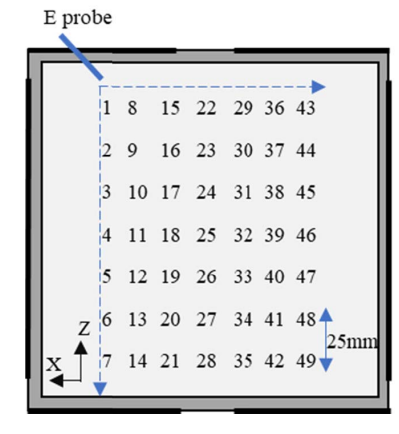


Fig. 4. Experimental validation of the E-field distribution using an E-field probe at different locations of the generator.

B. Experimental Validation of the Design

To experimentally validate the E-field distributions inside the generator, an E-field probe (Easy4MRI, ZMT) was placed inside the generator at 49 locations (at the vertical center slice of the gel) as shown in Fig. 4. These 49 positions were chosen with a step size of 25 mm along the *x*- and *z*-directions. The E-field generator was filled with 90-mm gel and the E-field probe was placed 45 mm under the gel surface.

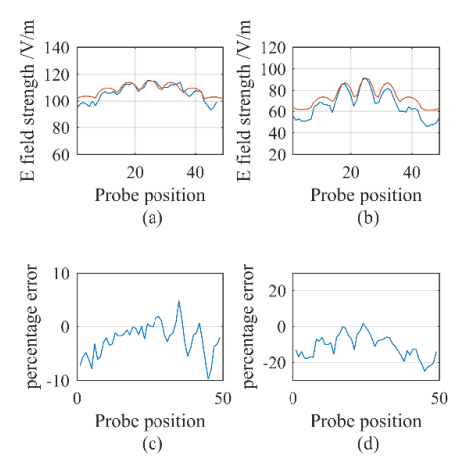


Fig. 5. Comparison of the measured and calculated E-fields inside the generator at 49 locations. (a) E-field at 64 MHz. (b) E-field at 128 MHz. The blue lines in (a) and (b) are the simulation and the red lines are the experimental results. (c) and (d) Relative errors for 64 and 128 MHz.

Comparisons of the E-fields obtained by the direct measurement and simulation are shown in Fig. 5. All the results shown here are for a net input power of 32.5 W for 64 MHz and 13.8 W for 128 MHz. Using these power levels, the E-field at the center of the generator will be similar to those at the ASTM recommended device testing location when a whole-body averaged phantom SAR of 2 W/kg is used. In the simulation, the input power is calculated using the S-parameter from the source sensors; the measurements are calibrated using the calorimetry method as suggested in [14] and [16]. As clearly shown in Fig. 4, the results obtained by experimental measurements were in good agreement with those from the simulations for both the 1.5- [see Fig. 3(a)] and 3-T [see Fig. 3(b)] systems. Such results validated our design.

C. Calibrations of the Dual-Frequency E-Field Generator

Two calibration procedures should be used to ensure the local E-field in the generator will be similar to that in the ASTM phantom. The first calibration procedure is referred to as the input power calibration which follows the calorimetry procedure described in [14] and [16]. The second calibration procedure follows the procedure of local exposure estimation based on [14].

For the input power calibration, we performed the following steps.

- 1) Fill the E-field generator with 90-mm saline (not gelled) with a relative permittivity of 78, an electrical conductivity of 0.47 S/m, and a weight of 6.85 kg.
- Cover the E-field generator with a thermal insulation lid to avoid evaporation and cooling of the saline which can produce a measurement error; leave the lid on the top of the E-field generator.
- 3) Measure the temperature at the center of the saline using a fiber probe until the temperature is stable (variation less than ± 0.5 °C).
- 4) Cover the entire system with thermal insulation material and apply the power for 900 s.
- 5) Stop the power input, quickly stir the saline, and measure the saline temperature rise with a fiber probe.

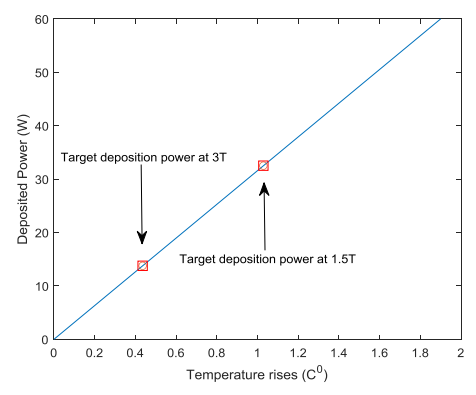


Fig. 6. Calibration curve to estimate the input power based on the calorimetry method.

6) Calculate the total deposited power in the saline using

$$P = c * m * \frac{\Delta T}{\Delta t}$$

where c is the specific heating capacity of the saline, c = 4150 J/kg/K, m is the mass of the saline which is 6.85 kg, ΔT is the temperature rise of the saline, and Δt is the heating time which is 900 s.

Based on the procedure described above, one can generate the required power following the calibration curve as shown in Fig. 6. As shown in Fig. 6, the target deposition power inside the phantom should have corresponding temperature rises around 1.03 °C at 64 MHz and 0.45 °C at 128 MHz to generate an incident E-field of 111 V/m at 64 MHz and 91 V/m at 128 MHz.

In addition, a local exposure calibration should also be performed per [14] using a 3.2 mm \times 10 cm titanium-alloy rod. Due to potential signal source drift and power amplifier variation between each experiment, the incident E-field at the center location of the generator can have slight variation. These variations should be captured through local exposure measurements. Therefore, before each device measurement, a five-step local energy calibration procedure as described in [14] should be performed. In the test, the gelled saline should be used to fill the E-field generator to 90 mm. Temperature rises for 6 min are measured near both ends of the titanium-alloy rod. The local SAR estimations (in terms of W/kg) should be estimated by $\Delta T_{360}/1.3$ at 64 MHz and $\Delta T_{360}/1.45$ at 128 MHz.

III. NUMERICAL STUDIES OF RF-INDUCED HEATING FOR IMDS

To show the equivalency of the RF-induced heating measurement between the E-field generator and the ASTM standard test system, two sets of IMDs were placed inside the E-field generator and the ASTM phantom (driven by an MRI RF coil). For the purpose of comparison, the 1-g averaged SAR was assessed [31]. During the RF-induced heating measurements in the E-field generator, the IMDs were placed at the center of the E-field generator, with the long axis of all devices aligned with the z direction.

The two device families used in this investigation are shown in Fig. 7. The first IMD family consists of fully threaded compression screws of different lengths and diameters. The second IMD family consists of plates and screws

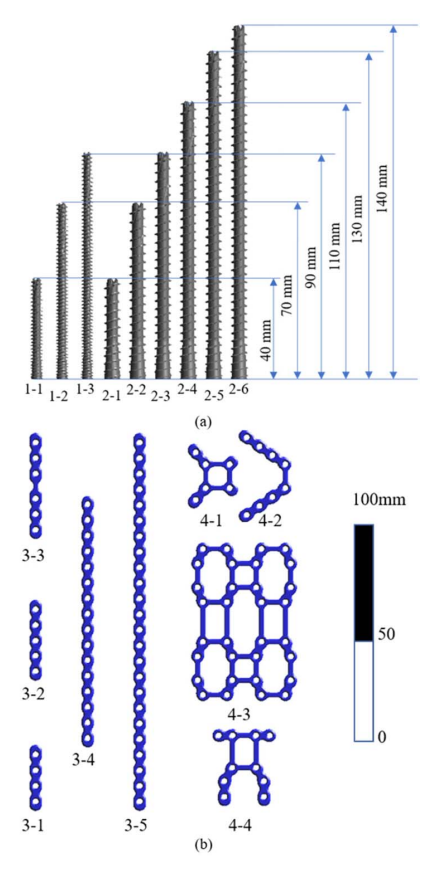


Fig. 7. Simulation models of (a) standalone screws and (b) plate system family.

from a typical trauma product. Nine plates with different dimensions were loaded with different numbers of screws.

In the RF-induced heating measurements using the ASTM phantom and an RF coil, the MRI RF coils were the MITS 1.5-T system (ZMT) and a standard commercial 3-T RF coil. The dimensions of these coils are given in Table II. In addition, two generic coil models were also used in the simulations. The simplified generic coils models were referred to as H8 coils [32]. They have hard current excitations on the legs of the coils. By varying the phase of those sources, the circular polarized (CP) mode can be generated. The dimensions of all physical and generic coils are shown in Table II.

An illustration of those coils is shown in Fig. 8(a) and (b). The comparisons of the simulation results for RF-induced energy near the devices are shown in Fig. 9, and all the SAR values shown in Fig. 9 were spatially averaged over a mass of 1 g. The input power of the ASTM system is normalized to

TABLE II
DIMENSIONS OF THE COILS USED IN THE SIMULATION

	1.5T	3T	1.5T	3T
	Physical	Physical	Generic	Generic
Coil radius (mm)	350	305	315	315
Coil length (mm)	650	550	650	650
Shielding radius (mm)	425	320	N/A	N/A
Shielding length (mm)	850	1450	N/A	N/A
Number of legs	16	16	8	8
Excitation type	IQ	IQ	Н8	Н8

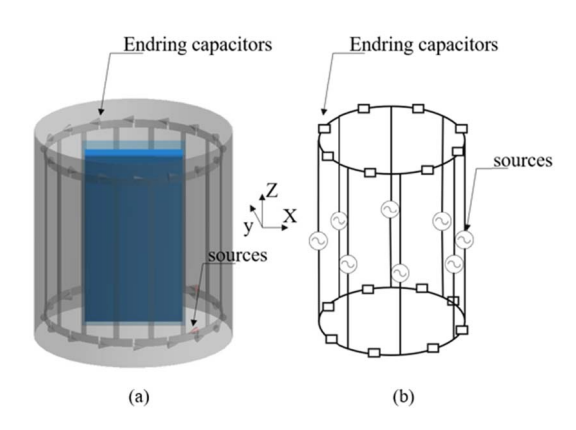


Fig. 8. (a) Typical birdcage coil used for MRI scanning. (b) Simplified generic coil H8 (hybrid eight-port generic coil).

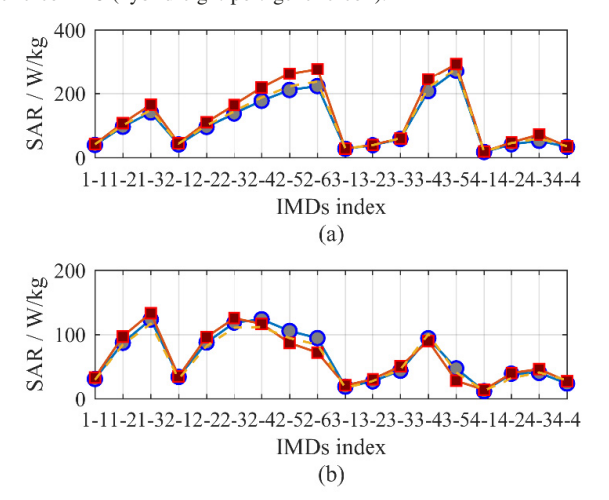


Fig. 9. Comparison of 1-g averaged SAR values in the simulation for (a) screw family and plate system for the 1.5-T MRI (64 MHz) and (b) screw family and plate system for the 3-T MRI (128 MHz); the blue solid line with the circles is for the ASTM standard test, red solid line with square is for the E-field generator, and the dashed line is for the ASTM standard test.

a whole-body averaged SAR of 2 W/kg. The results obtained from the E-field generator were calibrated to the incident E-field at the device test location inside the ASTM phantom. As clearly shown in Fig. 9, the E-field generator can produce similar energy deposition near the devices as those produced in the standard ASTM phantom.

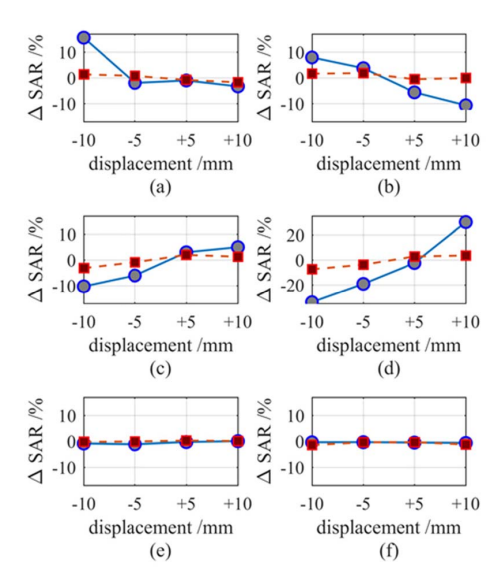


Fig. 10. SAR sensitivity of the screw family with respect to positioning error along (a) and (b) *x*-direction at 64 and 128 MHz, (c) and (d) *y*-direction at 64 and 128 MHz. (e) and (f) *z*-direction at 64 and 128 MHz. The blue solid line indicates data in the ASTM phantom, while the red dashed line indicates data for the E-field generator.

A sensitivity analysis was then performed to understand the impact the device positioning error has on the energy deposition near the IMDs for both the ASTM method and the E-field generator. For the worst case heating IMDs from each family, the IMDs are moved away from the center -10, -5, 5, and +10 mm along the x-, y-, and z-axes. The EM simulations were performed for the E-field generator and the ASTM phantom. Fig. 10 shows the results for screws 2-6 at 64 MHz and screws 1-3 at 128 MHz. Fig. 11 shows the results for plates 3-5 at 64 MHz and plates 3-4 at 128 MHz. As we can clearly see from these data, the newly designed E-field generator has similar sensitivity of the device positioning error along the z-direction as the ASTM phantom. However, the device positioning errors in the E-field generator along the x- and y-directions are much smaller than in the ASTM phantom. Overall, the E-field generator clearly outperforms the ASTM phantom in measurement uncertainty, power consumption, simplicity, size, and price.

IV. EXPERIMENTAL VALIDATION OF TEMPERATURE RISES

Based on the design presented above, a prototype of the E-field generator was developed as shown in Fig. 12. IMDs were placed inside this test generator and the RF-induced heating was measured. In all measurements, the temperature probes were placed at the maximum heating location based on the modeling results. For comparison, the thermal simulations were also obtained using Pennes' bioheat-based thermal solver in SEMCAD X. In both modeling and measurement, the RF power was turned on for 15 min. Temperature rises in both modeling and measurements are shown in Table III. All the results are normalized to a whole-body averaged SAR of 2 W/kg for the ASTM phantom. For the E-field generator, the input power is chosen to generate an equivalent E-field. In both settings, the incident E-field at the device test location was 111 V/m at 64 MHz and 91 V/m at 128 MHz.

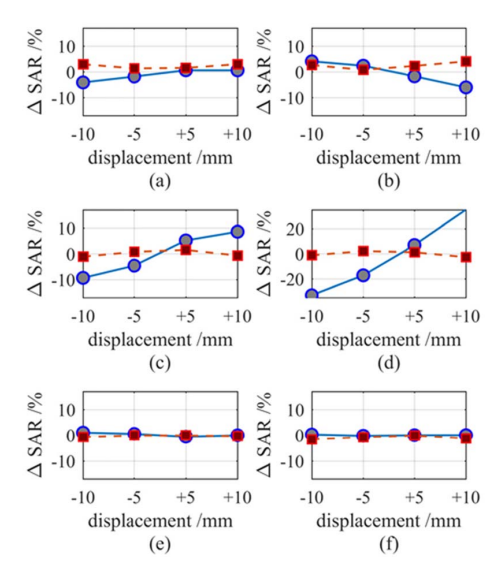


Fig. 11. SAR sensitivity of the plate system with respect to positioning error along (a) and (b) *x*-direction at 64 and 128 MHz, (c) and (d) *y*-direction at 64 and 128 MHz, (e) and (f) *z*-direction at 64 and 128 MHz. The blue solid line indicates data in the ASTM phantom, while the red dashed line indicates data for the E-field generator.

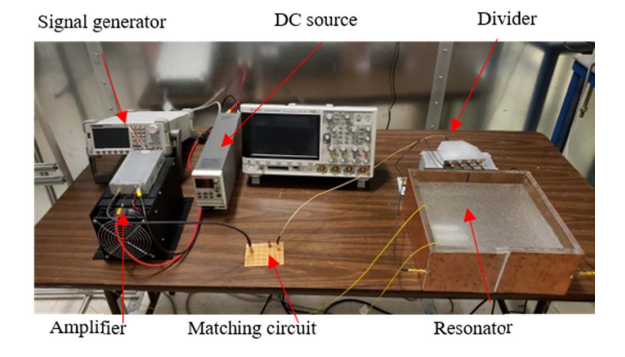


Fig. 12. Experimental setup for the E-field generator validation.

As shown in Table III, the measured temperature rises are consistent with the results from the simulations at both frequencies for both the E-field generator and the ASTM phantom. As shown in Table III, relatively large errors were observed for devices longer than the 1/2 wavelength, which will be explained in Section V.

V. DISCUSSION

From the results presented in Fig. 9, we can see that the induced SAR for most devices in the two IMD families at both 64 and 128 MHz shows a good agreement between the two different test systems. However, relatively large differences were observed for the longer devices 2-6, 3-4, and 3-5 at 64 MHz as shown in the numerical simulations (see Fig. 9) and the experimental experiments (see Table III). Such relatively large differences are due to the E-field variations along the z-direction, as well as the potential interaction between the IMD and the E-field generator. In the ASTM phantom, the E-field along the z-direction has a better uniformity than in the E-field generator since the E-field generator uses higher order modes. To achieve better agreement between the E-field generator and the ASTM phantom, the z-direction of the E-field generator can be extended which will lead to a better E-field uniformity. Currently, the RF-induced heating of the

TABLE III

COMPARISON OF THE MEASURED AND SIMULATED TEMPERATURE RISES
FOR BOTH 1.5 AND 3 T

1.5T (64 MHz)	E-field generator			ASTM phantom		
Part Number	Modeli ng ΔT/°C	Measur ed ΔT/°C	Differen ce/%	Modeli ng ΔT/°C	Measur ed ΔT/°C	Differe nce /%
1-3	9.85	8.55	15.21	7.96	8.19	-2.76
2-4	11.96	11.13	7.48	9.38	9.34	0.48
2-6	15.36	15.22	0.91	11.8	10.79	9.37
3-4	14.08	13.01	8.23	11.8	10.10	16.86
3-5	16.68	15.24	9.41	15.3	12.60	21.42

3T (128 MHz)		E-field generator			ASTM phantom		
Part Number	Modeli ng ΔT/°C	Measur ed ΔT/°C	Differen ce/%	Modeli ng ΔT/°C	Measur ed ΔT/°C	Differen ce /%	
1-3	7.76	6.73	15.29	7.22	7.86	-8.14	
2-4	6.33	5.58	13.38	6.58	6.55	0.48	
2-6	4.05	3.27	23.88	4.66	3.95	18.03	
3-4	5.21	4.59	13.43	5.43	6.98	-22.19	
3-5	1.82	1.70	7.06	2.97	2.60	14.23	

10-cm titanium rod is used to calibrate the local exposure. Using this calibration method, we find that for an IMD with a maximum length of less than 15 cm, the results obtained in the ASTM phantom and the E-field generator agree very well with each other. This agrees with the ASTM standard requirement that a 15-cm uniform incident E-field should be generated. Alternatively, one can develop better calibration parameters so that the averaged E-field along the z-direction is considered as a function of device length. Using this calibration, a better agreement can be achieved. However, this is beyond the current calibration procedure described in the ASTM standard.

From the results shown in Figs. 10 and 11, we can see that the IMD positioning error along the z-direction would lead to negligible RF-induced heating differences. However, such differences can be magnified for positioning errors along the x-and y-directions in the ASTM phantom. As clearly indicated in Figs. 10 and 11, a positioning error of 5 mm along the x- or y-direction in the ASTM phantom can change the induced SAR by 15%. Such variation can increase to 30% with a 10-mm positioning error along with these two directions. However, such a positioning error has almost no impact on the RF-induced heating when the E-field generator is used. The newly designed system can provide more consistent measurement results since the heating measurement is not very sensitive to the positioning error along all three directions. Based on these observations and a current side length of 30 cm, we observe that when the IMD overall length is less than one half of the incident field wavelength, all the results from measurement and modeling inside the ASTM phantom and the E-field generator agree well with each other.

Apart from the advantage of the measurement stability, the novel uniform E-field generator integrates both 1.5-T testing and 3-T testing into a single system without the need of an RF coil. In addition, using clinical, or clinically

equivalent, MRI RF coils would require a large shielded room, a high-power amplifier, and a large footprint for the equipment. The novel uniform E-field generator has much smaller dimensions and requires less than 100-W input power. This allows the E-field generator to become a desktop test system and an extremely useful alternative for IMDs MRI RF-induced heating measurements.

VI. CONCLUSION

In this article, we present a novel design of a uniform E-field generator. The design was guided by the cavity model and validated using numerical methods. Experimental validations of the design were performed by measuring the E-field distribution within the generator and comparing it to the simulation results. Two sets of IMD families were placed inside the E-field generator and the ASTM phantom for both modeling and measurement studies. From these studies, we observed highly correlated results for both frequencies 64 and 128 MHz. In addition, the measured RF-induced heating is less sensitive to device positioning errors in the E-field generator. Compared to the conventional ASTM method using an RF coil and the ASTM phantom for testing, this novel E-field generator has a significant advantage in terms of low cost, low operation power, ease of operation, and most importantly, integration of 1.5- and 3-T RF heating tests into a single desktop system. This provides us with a better alternative to evaluate the RF-induced heating of IMDs under MRI exposure. It is observed that when the device length is less than one half of the incident field wavelength, all the results from measurement and modeling inside the ASTM phantom and the E-field generator agree within the combined uncertainty of 25%.

ACKNOWLEDGMENT

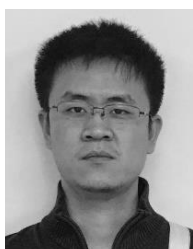
The mention of commercial products, their sources, or their use in connection with material reported herein is not to be construed as either an actual or implied endorsement of such products by the Department of Health and Human Services. The findings and conclusions in this article have not been formally disseminated by the Food and Drug Administration and should not be construed to represent any agency determination or policy.

REFERENCES

- J. Tian and D. Shrivastava, "In vivo radiofrequency heating in a 3T scanner," Theory and Applications of Heat Transfer in Humans, vol. 2. Hoboken, NJ, USA: Wiley, 2018, pp. 621–630.
- [2] T. Kawamura, K. Saito, S. Kikuchi, M. Takahashi, and K. Ito, "Specific absorption rate measurement of birdcage coil for 3.0-T magnetic resonance imaging system employing thermographic method," *IEEE Trans. Microw. Theory Techn.*, vol. 57, no. 10, pp. 2508–2514, Oct. 2009.
- [3] J. Liu, J. Zheng, Q. Wang, W. Kainz, and J. Chen, "A transmission line model for the evaluation of MRI RF-induced fields on active implantable medical devices," *IEEE Trans. Microw. Theory Techn.*, vol. 66, no. 9, pp. 4271–4281, Sep. 2018.
- [4] S. Feng, R. Qiang, W. Kainz, and J. Chen, "A technique to evaluate MRI-induced electric fields at the ends of practical implanted lead," *IEEE Trans. Microw. Theory Techn.*, vol. 63, no. 1, pp. 305–313, Jan. 2015.
- [5] J. A. Nyenhuis, S. M. Park, R. Kamondetdacha, A. Amjad, F. G. Shellock, and A. R. Rezai, "MRI and implanted medical devices: Basic interactions with an emphasis on heating," *IEEE Trans. Device Mater. Rel.*, vol. 5, no. 3, pp. 467–479, Dec. 2005.
- [6] J. A. Erlebacher, P. T. Cahill, F. Pannizzo, and R. J. R. Knowles, "Effect of magnetic resonance imaging on DDD pacemakers," *Amer. J. Cardiol.*, vol. 57, no. 6, pp. 437–440, Feb. 1986.

- [7] A. M. Sawyer-Glover and F. G. Shellock, "Pre-MRI procedure screening: Recommendations and safety considerations for biomedical implants and devices," *J. Magn. Reson. Imag.*, vol. 12, no. 1, pp. 92–106, 2000.
- [8] J. D. Poorter, C. D. Wagter, Y. D. Deene, C. Thomsen, F. Ståhlberg, and E. Achten, "Noninvasive MRI thermometry with the proton resonance frequency (PRF) method: *In vivo* results in human muscle," *Magn. Reson. Med.*, vol. 33, no. 1, pp. 74–81, Jan. 1995.
- [9] P. Ehses et al., "MRI thermometry: Fast mapping of RF-induced heating along conductive wires," Magn. Reson. Med., vol. 60, no. 2, pp. 457–461, Aug. 2008.
- [10] Magnetic Resonance Imaging (MRI). Accessed: Oct. 17, 2020. [Online]. Available: https://www.stryker.com/us/en/portfolios/neurotechnology-spine/neurovascular/embolization/test.html
- [11] Risks Associated With Magnetic Resonance Imaging (MRI) of Patients With Hip and Knee Implants. Accessed: Oct. 17, 2020. [Online]. Available: https://www.jnjmedicaldevices.com/sites/default/files/user_uploaded_assets/pdf_assets/2019-12/MRI%20Safety%20Brochure.pdf
- [12] C. M. Collins et al., "Temperature and SAR calculations for a human head within volume and surface coils at 64 and 300 MHz," J. Magn. Reson. Imag., vol. 19, no. 5, pp. 650–656, 2004.
- [13] R. Yang, J. Zheng, W. Kainz, and J. Chen, "Numerical investigations of MRI RF-induced heating for external fixation device in TEM and birdcage body coils at 3 T," *IEEE Trans. Electromagn. Compat.*, vol. 60, no. 3, pp. 598–604, Jun. 2018.
- [14] Standard Test Method for Measurement of Radio Frequency Induced Heating on or Near Passive Implants During Magnetic Resonance Imaging, document ASTM F2182-11a, 2019.
- [15] D. Li et al., "An efficient approach to estimate MRI RF field induced in vivo heating for small medical implants," IEEE Trans. Electromagn. Compat., vol. 57, no. 4, pp. 643–650, Aug. 2015.
 [16] Standard Test Method for Measurement of Radio Frequency Induced
- [16] Standard Test Method for Measurement of Radio Frequency Induced Heating on or Near Passive Implants During Magnetic Resonance Imaging, document ASTM F2182-11a, 2011.
- [17] Y. Liu, J. Chen, F. G. Shellock, and W. Kainz, "Computational and experimental studies of an orthopedic implant: MRI-related heating at 1.5-T/64-MHz and 3-T/128-MHz," J. Magn. Reson. Imag., vol. 37, no. 2, pp. 491–497, Feb. 2013.
- [18] S. McCabe and J. Scott, "A novel implant electrode design safe in the RF field of MRI scanners," *IEEE Trans. Microw. Theory Techn.*, vol. 65, no. 9, pp. 3541–3547, Mar. 2017.
- [19] S. M. Park et al., "Gelled versus nongelled phantom material for measurement of MRI-induced temperature increases with bioimplants," *IEEE Trans. Magn.*, vol. 39, no. 5, pp. 3367–3371, Sep. 2003.
- [20] H. S. Ho, "Safety of metallic implants in magnetic resonance imaging," J. Magn. Reson. Imag., vol. 14, no. 4, pp. 472–477, 2001.
- [21] F. G. Shellock, "Magnetic resonance safety update 2002: Implants and devices," J. Magn. Reson. Imag., vol. 16, no. 5, pp. 485–496, Nov. 2002.
- [22] P. Nordbeck et al., "Measuring RF-induced currents inside implants: Impact of device configuration on MRI safety of cardiac pacemaker leads," Magn. Reson. Med., vol. 61, no. 3, pp. 570–578, Mar. 2009.
- [23] P. Nordbeck et al., "Spatial distribution of RF-induced E-fields and implant heating in MRI," Magn. Reson. Med., vol. 60, no. 2, pp. 312–319, Aug. 2008.
- [24] Road Vehicles—Vehicle Test Methods for Electrical Disturbances From Narrowband Radiated Electromagnetic Energy, ISO Standard 11451-2, 2005
- [25] V. Rodriguez, "Analysis of large E field generators in semi-anechoic chambers used for full vehicle immunity testing: Numerical and measured results," in *Proc. IEEE Int. Symp. Electromagn. Compat.*, Dec. 2014, pp. 681–684.
- [26] J. S. McLean, "Electric field generator incorporating a slow-wave structure," U.S. Patent 7656167, Feb. 2, 2010.
- [27] C. Groh, J. P. Karst, M. Koch, and H. Garbe, "TEM waveguides for EMC measurements," *IEEE Trans. Electromagn. Compat.*, vol. 41, no. 4, pp. 440–445, Nov. 1999.
- [28] Assessment of the Safety of Magnetic Resonance Imaging for Patients With An Active Implantable Medical Device, Standard ISO/TS 10974: 2018, Apr. 2018.
- [29] H. F. Chen and K. H. Lin, "A numerical analysis of antenna factor of Bilog antennas for normalized site attenuation and EMC measurement," in *Proc. IEEE Int. Symp. Electromagn. Compat.*, vol. 2, Aug. 2003, pp. 817–821.
- [30] D. M. Pozar, "Microstrip antenna coupled to a microstrip-line," *Electron. Lett.*, vol. 21, no. 2, pp. 49–50, Jan. 1985.
- [31] International Electrotechnical Commission (IEC), Medical Electrical Equipment—Part 2-33: Particular Requirements for the Basic Safety and Essential Performance of Magnetic Resonance Equipment for Medical Diagnosis, document IEC-60601-2-33, Geneva, Switzerland, 2010.

[32] E. Lucano *et al.*, "Assessing the electromagnetic fields generated by a radiofrequency MRI body coil at 64 MHz: Defeaturing versus accuracy," *IEEE Trans. Biomed. Eng.*, vol. 63, no. 8, pp. 1591–1601, Aug. 2016.



Shuo Song (Graduate Student Member, IEEE) received the B.S. degree in electrical engineering from the Huazhong University of Science and Technology, Wuhan, China, in 2016. He is currently pursuing the Ph.D. degree at the University of Houston, Houston, TX, USA, under Prof. J. Chen's advising.

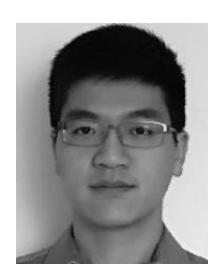
His current research interest lies in the MRI safety, especially human modeling and RF shimming.



Jianfeng Zheng (Member, IEEE) received the B.S. degree in electronic information engineering and the Ph.D. degree in electronic science and technology from Tsinghua University, Beijing, China, in 2002 and 2009, respectively.

He was an Assistant Researcher with the State Key Laboratory on Microwave and Digital Communications, Tsinghua University. Since 2012, he has been a Post-Doctoral Fellow with the Department of Electrical and Computer Engineering, University of Houston, Houston, TX, USA. His current research

interests include applied electromagnetics on biomedical applications, MRI RF safety, multiple-input and multiple-output (MIMO) channel measurements, and antenna arrays for MIMO communications.



Yu Wang received the B.S. degree from the University of Electronic Science and Technology of China, Chengdu, China, in 2016. He is currently pursuing the Ph.D. degree at the University of Houston, Houston, TX, USA.

His research interests include the application of computational modeling and experimental measurements aimed to evaluate the RF safety for patients with medical implants.



Qingyan Wang received the B.S. degree in electronics and information engineering from the Huazhong University of Science and Technology, Wuhan, China, in 2011 and the Ph.D. degree in electrical engineering from the University of Houston, Houston, TX, USA, in 2016.

Since 2016, he has been a Post-Doctoral Researcher with the University of Houston. His current research interests include applied electromagnetics on biomedical applications, magnetic resonance imaging radio frequency (RF) safety modeling, and RF measurement.



Wolfgang Kainz (Member, IEEE) received the M.S. degree in electrical engineering and the Ph.D. degree in technical science from the Technical University of Vienna, Vienna, Austria, in 1997 and 2000, respectively.

He worked with the Austrian Research Center, Seibersdorf, Austria. He joined the Foundation for Research on Information Technologies in Society (IT'IS), Zurich, Switzerland, as an Associate Director, where he worked on the development of *in vivo* and *in vitro* exposure setups for bioexperi-

ments. In 2004, he initiated the Virtual Family Project in co-operation with IT'IS and Prof. J. Chen from the University of Houston, Houston, TX, USA. He is currently a Research Biomedical Engineer with the Center for Devices and Radiological Health, U.S. Food and Drug Administration (FDA), Silver Spring, MD, USA. He has authored or coauthored more than 160

peer-reviewed articles and book chapters. His research interest is currently focused on the safety and effectiveness of medical devices and safety of humans in electromagnetic fields. This includes computational electrodynamics for safety and effectiveness evaluations using anatomical models of the human anatomy; magnetic resonance imaging safety; performance and safety of wireless technology used in medical devices; electromagnetic compatibility of medical devices; dosimetric exposure assessments from dc to light; and novel methods to computationally assess the safety and effectiveness of neuroprosthetics and therapeutic stimulation methods.

Dr. Kainz is a member of the Administrative Committee of the IEEE International Committee on Electromagnetic Safety and many international standard setting committees. He received the Prestigious FDA Award of Merit for exceptional leadership in performance in addressing issues of compatibility of medical devices during MRI by applying transparently scientific research to device regulation in 2010.



Stuart A. Long (Life Fellow, IEEE) was born in Philadelphia, PA, USA. He received the B.A. (magna cum laude) and M.E.E. degrees in electrical engineering from Rice University, Houston, TX, USA, in 1967 and 1968, respectively, and the Ph.D. degree in applied physics from Harvard University, Cambridge, MA, USA, in 1974.

He has been a Faculty Member with the Department of Electrical and Computer Engineering, University of Houston, Houston, for the past 47 years, where he was the Chair of the Department of Electri-

cal and Computer Engineering from 1981 to 1995, the Interim Dean of Honors College from 2008 to 2009, served as the Interim Vice-Chancellor and the Vice-President of research and technology transfer from 2010 to 2011, and is currently the Associate Dean of undergraduate research and Honors College. His research interests are in the broad area of applied electromagnetics and more specifically in microstrip and dielectric resonator antennas.

Dr. Long is a member of Phi Beta Kappa, Tau Beta Pi, Sigma Xi, and Commission B of URSI and was elected to membership in the Electromagnetics Academy in 1990. He was awarded the IEEE Millennium Medal in 2000, the IEEE Antennas and Propagation Society (AP-S) Outstanding Service Award in 2007, the IEEE AP-S John Kraus Antenna Award in 2014, and the IEEE AP-S Chen-To Tai Distinguished Educator Award in 2018. He was named as the first recipient of the University of Houston Career Teaching Excellence Award in 2009 and received the Esther Farfel Award in 2010, the highest faculty award given at the University of Houston. He served as an IEEE AP-S Distinguished Lecturer from 1992 to 1994. He was the Elected President of IEEE AP-S in 1996. He served on the IEEE Technical Activities Board, was the TAB Magazines Chair, a member of the Periodicals Review Committee from 1997 to 1999, and a Member-at-Large of the IEEE Publications Activities Board from 1998 to 2003, and served on the Spectrum Editorial Board from 2002 to 2005. He was elected to serve on the Board of Directors of IEEE for 2005-2006 as the Director of Division IV.



Ji Chen (Senior Member, IEEE) received the B.S. degree from the Huazhong University of Science and Technology, Wuhan, China, in 1989, the M.S. degree from McMaster University, Hamilton, ON, Canada, in 1994, and the Ph.D. degree from the University of Illinois at Urbana–Champaign, Urbana, IL, USA, in 1998, all in electrical engineering.

He is currently a Professor with the Department of Electrical Engineering, University of Houston, Houston, TX, USA. His research interests include microprocessor full chip-level interconnect extrac-

tion, wireless communication system-on-chip interconnect characterization, computer system electromagnetic compatibility/electromagnetic interference modeling, signal integrity analysis, and bioelectromagnetics with applications to MRI systems.

Dr. Chen was a recipient of the ORISE Fellowship in 2006 and the Motorola Engineering Award in 2000.